PHYSICAL REVIEW A **108**, 063108 (2023)

Visualizing molecular unidirectional rotation by a rotated weak-field polarization technique

Zhenzhong Lian,[1,2] Zhou Chen,[1,*] Juan Li,[1] Chuan-Cun Shu,[2,†] and Zhan Hu[1,3]

[1] *Institute of Atomic and Molecular Physics, Jilin University, Changchun 130012, China*
[2] *Hunan Key Laboratory of Super-Microstructure and Ultrafast Process, School of Physics, Central South University, Changsha 410083, China*
[3] *Advanced Light Field and Modern Medical Treatment Science and Technology Innovation Center of Jilin Province, Jilin University, Changchun 130012, China*

(Received 17 August 2023; accepted 5 December 2023; published 19 December 2023)

The observation of molecular rotational dynamics induced by ultrashort laser pulses is of both fundamental and practical importance. Here, we develop an extended weak-field polarization method that allows us to visualize the two-dimensional spatial rotation of molecules. By manipulating the polarization direction of the pump pulse, this method allows for characterizing the rotational dependence on the azimuth angle when a weak probe pulse is present. To demonstrate this experimental scheme, we examine two types of pump pulses: (1) a linearly polarized pulse and (2) temporally delayed double pulses polarized at an angle of $\pi/4$, which are respectively applied to gas-phase molecules N_2O at room temperature. The results show that this approach effectively captures the induced impulsive alignment and unidirectional rotation. By solving the time-dependent Liouville equation governing the molecules' behavior under the influence of the polarization-skewed pump pulses, we gain further insights into the mechanisms for generating unidirectional rotation. This work holds promising potential in the detection of two- and three-dimensional rotational dynamics of molecules like enantiomers and superrotors.

DOI: 10.1103/PhysRevA.108.063108

I. INTRODUCTION

Controlling microscopic quantum systems and their properties has long been a cornerstone in atomic, molecular, and optical physics (AMO). The emergence of laser techniques has provided a powerful means for manipulating molecular rotation through ultrashort laser pulses. This breakthrough has facilitated the creation of ensembles of molecules that are aligned and oriented, resulting in a wide range of applications encompassing photon ionization, high harmonic generation (HHG), and chemical reaction control [1–3]. Extensive theoretical and experimental endeavors have been dedicated to enhancing the level of alignment and fixing molecules in specific orientations [4–12]. In addition to transient alignment, tailored ultrashort pulses have unraveled fascinating phenomena, including superrotor and unidirectional rotation, sustained alignment, and rotational echo [10,13–24].

Considerable methods have been proposed to characterize the rotational motion and map the spatial angular distribution of the rotational wave packet. Usually, the expectation value of $\cos^2\theta$, where θ represents the angle between the molecular axis and a specific direction, is used to quantify the degree of alignment, providing one-dimensional spatial information only. However, to capture rotational motion such as three-dimensional (3D) alignment and unidirectional rotation, an additional dimension beyond $\cos^2\theta$ is required. A widely adopted approach for visualizing unidirectional rotation, rotational echo, and 3D alignment involves detecting the momentum of correlated molecular fragmentation following Coulomb explosion [25–31]. This technique directly reveals the angular distribution of the rotational wave packet. Another valuable tool for studying the three-dimensional characteristics of molecular rotational dynamics is the photoelectron and HHG spectra induced by rotationally excited molecules, providing insight into the complex nature of molecular rotation [32–36]. Furthermore, a method based on diffracted electron beam analysis has been proposed to reconstruct nuclear positions within the molecule [37,38]. Despite these methods' versatility and comprehensive applications, they are typically destructive and require a vacuum environment and low temperatures for conducting experiments.

Based on Raman-induced polarization spectroscopy, the weak-field polarization (WFP) method has been developed as a nondestructive and easily implementable technique for measuring molecular rotational motion in a less restrictive environment [39–42]. It has effectively detected impulsive alignment and rotational echoes in condensed environments [43–45]. The essential advantage of this optical method lies in its detection of the probe pulse, which is insensitive to the surrounding environment, thereby allowing for accurate measurements. However, most applications of the WFP method were limited to obtaining only one-dimensional information by characterizing the dependence of the polar angle θ. Recent advancements have demonstrated the feasibility of using all-optical techniques, such as employing a vortex plate, to image the probe pulse's polarization and capture the molecular orientation [46,47]. This represents a significant step towards imaging rotational motion optically. Furthermore, a more

---

[*] phy_cz@jlu.edu.cn
[†] cc.shu@csu.edu.cn

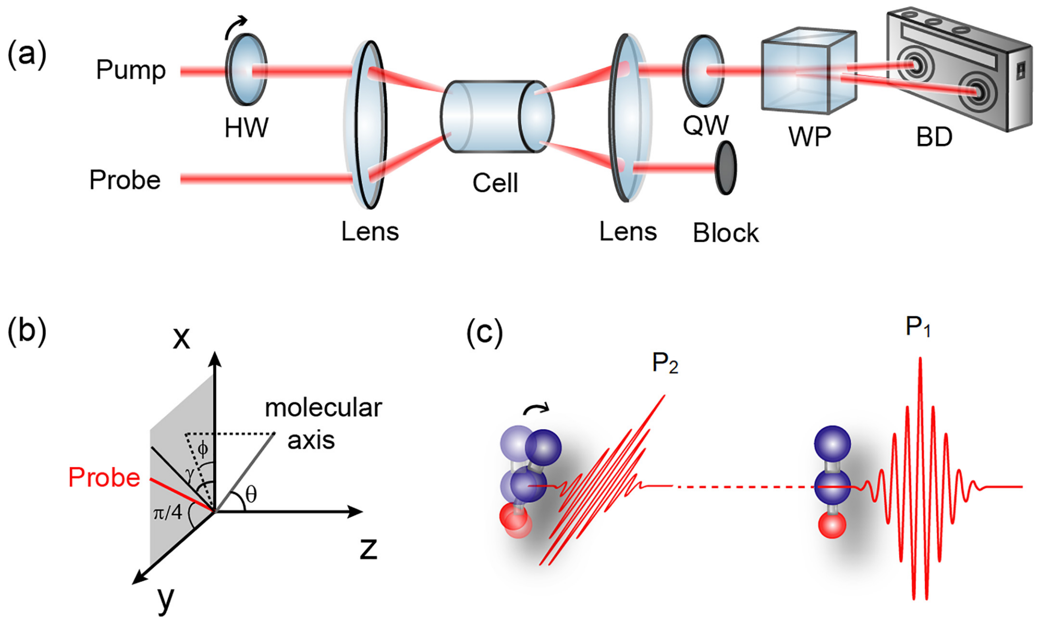

FIG. 1. (a) Schematic of experimental setup for detecting the rotational motion of the molecules. HW, half waveplate; QW, quarter waveplate; WP, Wollaston prism; BD, balanced detector. (b) Different angles adopted in current paper. See details in the text. (c) A pair of time delayed, polarization-skewed pump pulses that excite the molecule into unidirectional rotation.

straightforward approach has been proposed, which involves varying the relative angle between the linearly polarized pump and probe pulses to image the rotational wave packet [48]. It is important to note that no experimental reports have utilized this particular approach to obtain spatial-temporal information about molecular rotational motion. Utilizing such methodologies could inspire further research and development of an optical experimental technique that can effectively measure the spatial angular distribution of molecules and image complex rotational motion.

In this work, we introduce a rotated WFP method that allows for the observation of two-dimensional spatial information about molecules. This is achieved by incorporating a polarization-varied pump pulse and a weak probe pulse. Our experimental setup enables us to detect the unidirectional rotation of N_2O molecules induced by polarization-skewed pulses at room temperature, which expands the capabilities of the WFP method to gain insights into the spatial aspects of molecular rotations. To further analyze and understand the rotational dynamics, we numerically solve the time-dependent Liouville equation to simulate the rotational dynamics of molecules induced by such schemes. Our experimental results combined with numerical simulations offer an alternative approach to visualize and study intricate molecular rotational motion at room temperature.

We organize the paper as follows. In Sec. II, we describe the details of the experimental setup used to implement the rotated WFP method, including the femtosecond pump pulse, weak probe pulse, and the detection scheme. The theoretical simulation method for the numerical solution of the time-dependent Liouville equation is also explained. In Sec. III, we present the experimental findings of imaging the impulsive alignment and unidirectional rotation of N_2O molecules using the rotated WFP method, compared with the corresponding theoretical simulation results, providing a comprehensive understanding of the observed phenomena. We summarize the essential findings and their implications in Sec. IV, highlighting the significance of the rotated WFP method for visualizing complex molecular rotational motion at room temperature.

II. METHODS FOR EXPERIMENT AND SIMULATION

The scheme of our experimental setup is illustrated in Fig. 1(a). We utilize a femtosecond pump pulse to excite the molecules in the cell, inducing a superposition of rotational states known as a rotational wave packet (RWP). A weak probe pulse, with a variable time delay, passes through the ensemble of the RWP and experiences the anisotropic distribution of molecules. As a result, the intensity of the probe pulse varies in different polarization directions. By measuring this intensity difference, the information about the angular distribution of the RWP can be obtained. To measure this intensity difference, we employ a heterodyne detection scheme, which involves sending the weak probe pulse through a quarter wave plate and a Wollaston prism [41]. Two orthogonal polarization components of the probe will separate in space and be detected by a balanced detector. In standard WFP detection experiments, the pump pulse is polarized in a fixed direction, while a weak probe pulse rotated by a certain angle of $\pi/4$ is applied to the pump pulse [39]. Instead of using a fixed angle between the polarization of the pump and probe pulses, we here gradually change the polarization direction of the pump pulse using a motorized half-wave plate. As discussed below, this change in the relative angle between the polarization of the pump and probe pulses allows us to detect two-dimensional spatial information about the RWP and visualize the unidirectional rotation induced by the double-skewed pump pulses.

As depicted in Fig. 1(b), we take the laser propagation direction as the z axis in the space-fixed coordinate, and the electric field vectors of both the pump and probe pulses therefore lie in the x-y plane. To describe the orientation of the molecular axis, we introduce the polar angle θ to the z axis and the azimuth angle ϕ to the x axis. It is important to note that we consider a linear molecule for this study. As we rotate the half-wave plate, the angle by which the polarization of the pump pulse rotates is denoted as γ. The polarization of the probe pulse remains fixed at an angle of $\pi/4$ to the x axis.

According to the WFP detection method [39], the intensity variation of the probe pulse after passing through the sample is attributed to the probe-induced dipole moment, denoted as $\mu_{\rm ind} = \alpha \cdot \vec{E}_{\rm pr}$, where α represents the polarizability tensor of the molecule and $\vec{E}_{\rm pr}$ is the electric field of the probe pulse. The detected intensity $I_{\rm sig}$ at a specific direction $\vec{n}$, emitted by this dipole, is proportional to the square magnitude of the trace of $\vec{n} \cdot \vec{\mu}_{\rm ind}\rho$:

$$I_{\rm sig} \propto |{\rm Tr}(\vec{n} \cdot \vec{\mu}_{\rm ind}\rho)|^2, \tag{1}$$

where ρ corresponds to the density matrix of the RWP, with matrix elements $|J, m\rangle\langle J', m'|$. The rotational eigenstate $|J, m\rangle$, where quantum numbers J, m are associated with the angular momentum and its projection on the z axis, can be represented by the spherical harmonic function $Y_{Jm}(\theta, \phi)$. By utilizing the rotation matrix R to describe the expression mentioned above in the molecular body-fixed coordinate system [2], the projection of $\vec{\mu}_{\rm ind}$ onto $\vec{n}$ can be expressed as

$$\vec{n} \cdot \vec{\mu}_{\rm ind} \propto \sin^2\theta \cos^2\phi \Delta\alpha, \tag{2}$$

where $\Delta\alpha$ denotes the difference between the parallel and perpendicular components of the polarizability tensor $\alpha_\parallel$ and $\alpha_\perp$.

As we gradually rotate the polarization of the pump pulses by γ, we represent the matrix density induced as ρ^γ and the signals will turn into

$$\begin{aligned} I_{\rm sig}(t,\gamma) &\propto \left| \sum_{Jm} \rho^{\gamma}_{JmJ'm'}(t) \int \sin\theta {\rm d}\theta {\rm d}\phi Y_{Jm}(\theta,\phi) \right. \\ &\quad \left. \times Y^*_{J'm'}(\theta,\phi) \sin^2\theta \cos^2\phi \Delta\alpha \right|^2 \\ &= \left| \sum_{Jm} \rho^{0}_{JmJ'm'}(t) \int \sin\theta {\rm d}\theta {\rm d}\phi Y_{Jm}(\theta,\phi) \right. \\ &\quad \left. \times Y^*_{J'm'}(\theta,\phi) \sin^2\theta \cos^2(\phi-\gamma) \Delta\alpha \right|^2. \end{aligned} \tag{3}$$

It implies that the γ-dependent signal encodes the ϕ dependence of the rotational probability density. The rotational operator $\cos^2(\phi - \gamma)$ behaves as a δ function to project ϕ into a specific direction γ. By changing γ, coarse information of the angular distribution along ϕ can be obtained in addition to the degree of alignment. Therefore, the current scheme enables us to detect the unidirectional rotation, where the axial symmetry of the molecular rotation has been destroyed. As depicted in Fig. 1(c), temporally delayed double pump pulses are used to induce unidirectional molecular rotation. When the second pump pulse is polarized in a different direction compared to the first one, it disrupts the axial symmetry of the rotational wave packet. Particularly, when the second pump pulse is applied around the impulsive alignment, it leads to the generation of unidirectional rotation [13].

In our experiment, a Ti: sapphire optical parametric chirped pulse amplification system is utilized to generate a transform-limited (TL) laser pulse with duration of 120 fs and central wavelength of 800 nm at a 1-kHz repetition rate. Two types of pump pulses are employed: (1) a single TL pulse and (2) temporally delayed double TL pulses with a tilted angle of $\pi/4$. The peak power density of each single TL pulse is $10^{12}\,{\rm W/cm^2}$. To acquire the signals $I_{\rm sig}(t, \gamma)$, a motorized delay stage and a half-wave plate mounted on a rotational stage are used to control the delay t and the polarization angle γ between the pump and probe pulses. The sample used in the experiment is N_2O. It has a rotational period $T_{\rm rev}$ of 39.9 ps. The experiment is conducted at room temperature $T = 295$ K and atmospheric pressure.

For numerical simulations, the time-dependent density matrix $\rho(t)$ of the system can be obtained by solving the quantum Liouville equation

$$i\hbar \frac{{\rm d}\rho(t)}{{\rm d}t} = [\hat{H}_0 + \hat{H}_{\rm I}, \rho(t)], \tag{4}$$

where the field-free Hamiltonian is $\hat{H}_0 = BJ(J+1)$ with the rotational constant B and the interaction Hamiltonian $\hat{H}_{\rm I}$ is given by

$$\hat{H}_{\rm I} = -\tfrac{1}{2}\Delta\alpha \sin^2\theta\left(\cos^2\phi E_x^2 + \sin^2\phi E_y^2 + 2\sin\phi\cos\phi E_x E_y\right), \tag{5}$$

with E_x and E_y represent the electric fields of the pump pulse along the x and y axes, respectively. The initial density matrix of the system at the initial time $t = t_0$ can be expressed as

$$\rho(t_0) = \sum_{J=0}^{J_{\max}} \sum_{m=-J}^{J} \frac{g_J}{Z} e^{-\frac{\hbar BJ(J+1)}{k_B T}} |Jm\rangle\langle Jm|, \tag{6}$$

where g_J represents the degeneracy of the nuclear spin, which is equal to 1 for both even and odd J states of N_2O [49]. The partition function Z is defined by

$$Z = \sum_{J,m} g_J \exp\left(\frac{\hbar BJ(J+1)}{k_B T}\right), \tag{7}$$

where k_B is the Boltzmann constant. In our simulation, we perform a weighted average of the initial states with a maximum value of $J_{\max} = 50$. This choice is sufficient by including 99.99% of the initial states.

III. RESULTS AND DISCUSSION

Using the scheme discussed above, we first measure and analyze the experimental results of the RWP induced by a single TL pump pulse, which creates a rotational wave packet in the N_2O molecule and thereby leads to time-dependent alignment and anti-alignment. Figure 2(a) shows the normalized experimental signals for $\gamma = 0$ and $\gamma = \pi/2$, which are symmetric to the baseline. The probe delay is extended to 41.5 ps, covering one rotational revival period of N_2O. The signals of full revival and half revival are clearly observed, in accordance with previous study [50]. Figure 2(b) displays the

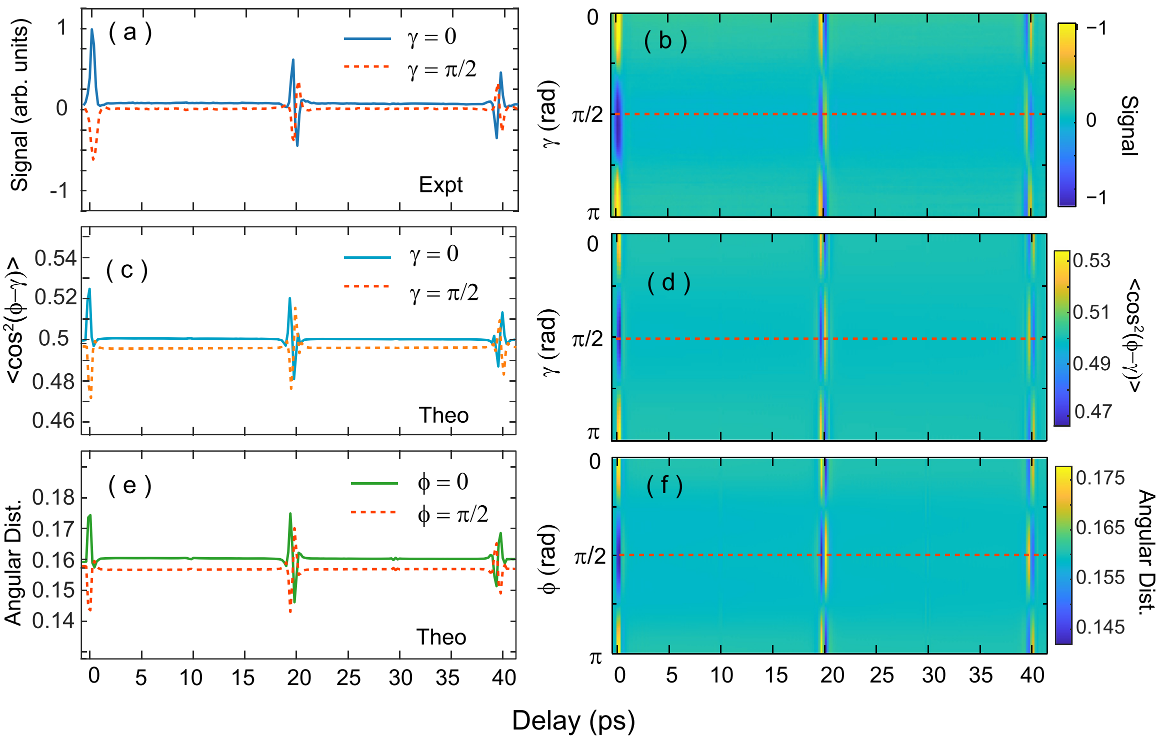

FIG. 2. Experimental and corresponding theoretical results of the RWP induced by single TL pump pulse. Normalized experimental results with the angle (a) $\gamma = 0$ and $\pi/2$ and from (b) 0 to π. Theoretical results of $\cos^2(\phi - \gamma)$ with (c) $\gamma = 0$ and $\pi/2$ and (d) from 0 to π. Theoretical calculation of the angular distribution with (e) $\phi = 0$ and $\pi/2$ and from (f) 0 to π.

detected signals as a function of the continuously changing γ from 0 to π. We can see that the signals tend to peak at $\gamma = 0$ and then at $\gamma = \pi/2$ around the half-revival period, indicating alignment and antialignment, respectively. The symmetrical structure about $\gamma = \pi/2$ suggests that the RWP transitions from alignment to antialignment without changing the direction of its symmetry axis.

The expectation value of $\cos^2(\phi - \gamma)$, which is proportional to the detected signal according to Eq. (3), is calculated to analyze further the experimental results. The results are shown in Figs. 2(c) and 2(d). Additionally, the corresponding angular distribution with respect to ϕ integrated over θ is also calculated to capture the actual motion of the RWP, as shown in Figs. 2(e) and 2(f). It can be observed that both the simulated signal and the angular distribution accurately reconstruct the experimental results under the given conditions. The detected signal provides information about the spatial distribution along ϕ and reveals the symmetry distribution as the RWP evolves.

As discussed in Ref. [48], the detailed information in the exact angular distribution cannot be reflected from the optical detection method. This is mainly because the measurement operator $\cos^2(\phi - \gamma)$ is less sharply peaked than a δ function. As depicted in the current work, the difference between the detected signal and the angular distribution is minor. This is due to that the number of the initial rotational states involved in our experiment is much bigger than the previous theoretical work [48]. During the third quarter revival period in Fig. 2(e), certain subtle features are present but are not detectable from the experimental signals. However, the most important features at the half and full revival time show no visible difference between the detected signal and the angular distribution. This suggests that our scheme is well suited for detecting the motion of molecular ensembles at high temperatures, where a greater number of initial rotational states are involved.

We also employ double skewed pump pulses polarized at an angle of $\pi/4$ and with a delay time of 40 ps to excite N_2O molecules. The second pump pulse is utilized to induce the aligned RWP at full revival to rotate in a specific direction, generating unidirectional rotation [26]. The detected signal of N_2O and the theoretical simulations are shown in Fig. 3, which follows the same layout as Fig. 2. The top plots represent the experimental results, while the middle and bottom plots depict the theoretical results of $\langle\cos^2(\phi - \gamma)\rangle$ and the angular distribution, respectively. The zero delay corresponds to the arrival time of the second pump pulse.

From Fig. 3(a) for $\gamma = 0$, we can observe that the structure of the signal is similar to that of the Fig. 2, indicating the transition of the molecular ensemble from alignment to antialignment around the half revival period and vice versa around the full revival period. However, the overall signals in Fig. 3(b) no longer exhibit symmetry about $\gamma = \pi/2$. Instead, the signal becomes tilted as the time progresses, indicating that the angular distribution of the RWP rotates in a preferred direction, different from the previous observation in Fig. 2(b). Thus, the second pump pulse induces unidirectional rotation of the RWP, leading to the observed tilt in the signal. This result is consistent with previous experiments utilizing the Coulomb explosion method to detect unidirectional rotation

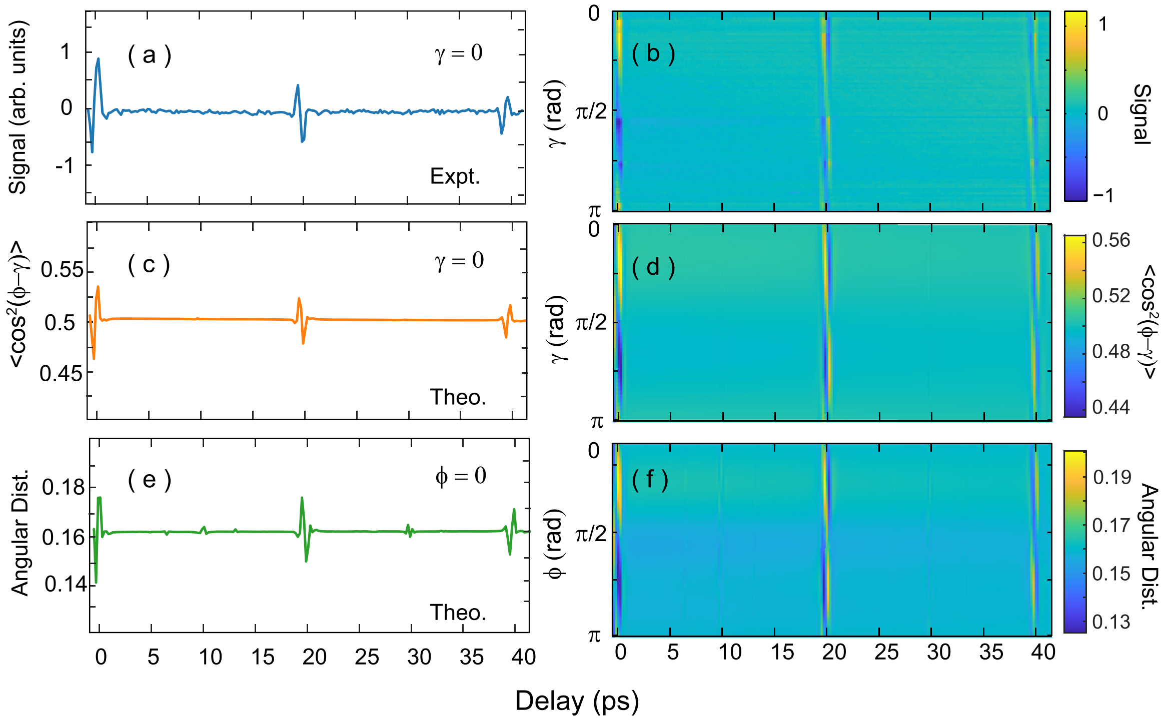

FIG. 3. Experimental and corresponding theoretical results of the RWP induced by a pair of time delayed, polarization-skewed TL pump pulses. Normalized experimental results with the angle (a) $\gamma = 0$ and $\pi/2$ and from (b) 0 to π. Theoretical results of $\cos^2(\phi - \gamma)$ with the angle (c) $\gamma = 0$ and $\pi/2$ and from (d) 0 to π. Theoretical calculation of the angular distribution with (e) $\phi = 0$ and $\pi/2$ and from (f) 0 to π.

[15,26]. The simulation results in Fig. 3 match the experimental results very well. The angular distribution of the RWP along ϕ in Fig. 3(f) also exhibits the same tilted pattern, confirming the capability of the current scheme to visualize unidirectional rotation. The slight difference between the detected signal and the angular distribution can be observed in the first and third quarter revival periods.

We conduct precise measurements around the half and full revival periods to gain a clearer view of the unidirectional rotation, employing a minor probe step of 13 fs. The experimental results are shown in the first row of Fig. 4 and the corresponding simulated angular distribution along the probe delay is displayed below. Figure 4(a) depicts the detected signal from 19 to 21 ps, revealing the unidirectional rotation around the half revival period. The corresponding angular distribution of the RWP is shown in Fig. 4(e). We extract experimental data at three different delays around 19.7 ps and plot them in polar graph in Fig. 4(b). As can be seen, the rotational wave packet aligns at approximately $\gamma = \pi/5$ with the delay of 19.6 ps and then rotates clockwise. The polar graph for the simulated angular distribution of ϕ in Fig. 4(f) also exhibits the same rotation. Based on the observed angle of rotation of the RWP around 19.7 ps, the experimental data indicate a transient angular velocity of about 10^{12} rad/s, which is consistent with the theoretical prediction (see details in the Appendix). The experimental results at the full revival also agree well with the theoretical simulations. The polar graphs in Figs. 4(d) and 4(h) indicate the clockwise rotation of the antialignment state around 39.7 ps. The experimental signals around the full revival become noisier due to decoherence of the RWP after 40 ps of free evolution. The signal asymmetry is closely related to the delay between the two pump pulses, which significantly affects the unidirectional rotation, transitioning it from clockwise to counterclockwise rotation [26].

We examine the population distribution of different J and m in Fig. 5 to understand the excitation process underlying the unidirectional rotation. Figure 5(a) illustrates the overall population distribution of different J and the average $\langle m\rangle(t) = \sum_{m=-J}^{J} m\rho_{JmJm}(t)$ for each J, in the beginning, after the first pump pulse, and after the second pump pulse. The populations of different J resemble a Boltzmann-like distribution, with little change after the excitation with the first and second pump pulses, as the pump intensity is moderate in the current work. The plot of $\langle m\rangle$ in Fig. 5(a) demonstrates an asymmetry that is responsible for the unidirectional rotation. Before applying the second pump pulse $\langle m\rangle$ remains zero for all J, indicating that the probabilities of exciting positive and negative m values are identical under a single linearly polarized pulse. However, $\langle m\rangle$ deviates from zero after interacting with the second pump pulse. For $J < 20$, $\langle m\rangle$ becomes negative, while for $J > 20$, $\langle m\rangle$ becomes positive, with a smooth change among different J values.

To further analyze the population changes of different m during the interaction with the pump pulses, we plot the population of different m ranging from -4 to 4 for $J = 16$, which dominates the initial distribution, as a function of time around the first and second pump pulses. These results, along with the corresponding pulse envelopes, are shown in Figs. 5(b) and 5(c). In Fig. 5(b), the population of different m values starts equal at the beginning. During the interaction with the first pump pulse, we observe a decrease in the populations of various $|m|$ states, making them distinguishable from each

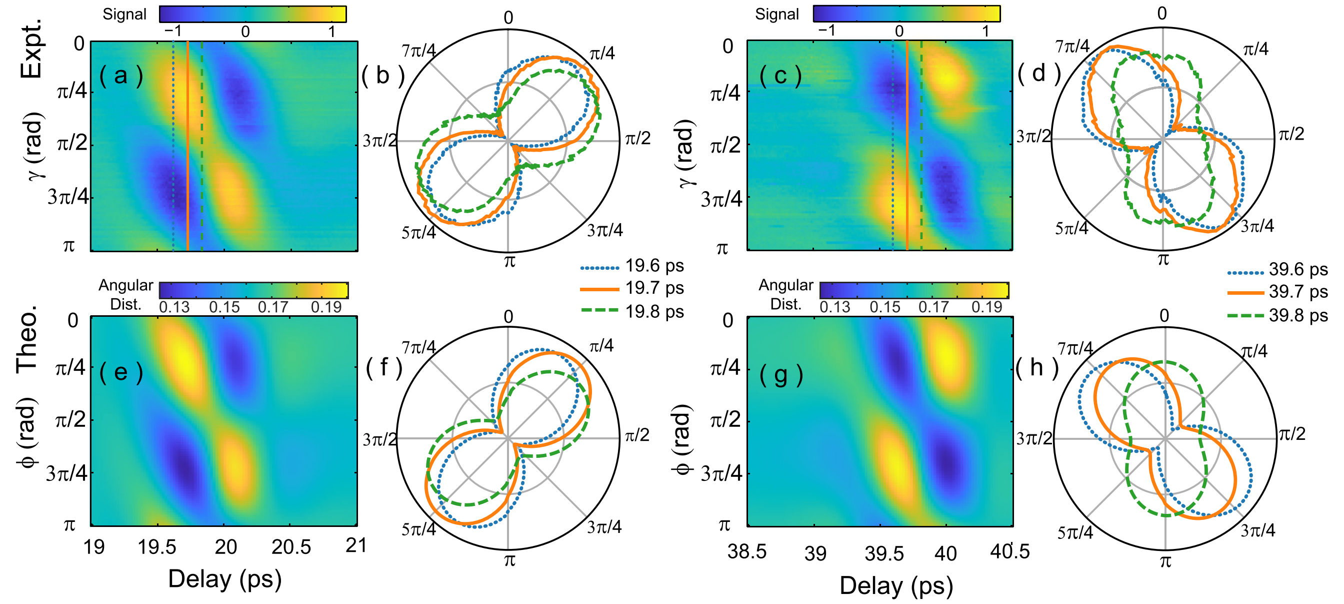

FIG. 4. The experimental signal and simulated angular distribution of unidirectional rotation around half and full revival. (a) Experimental and (e) simulated results around half revival. Polar plots of (b) the detected signal and (f) simulated angular distribution at 19.6, 19.7 and 19.8 ps. (c) Experimental and (g) simulated results around full revival. Polar plots of the (d) detected signal and (h) simulated angular distribution at 39.6, 39.7, and 39.8 ps.

other. However, the populations of $\pm m$ states with the same m remain equal by the interaction with the pump pulse. The final populations after the interaction with the first pump pulse shown in Fig. 5(b) belong to $|m| = 0$, 1, 2, 3, and 4 in a descending order. When the system interacts with the second pump pulse, the populations of $\pm m$ start to diverge,

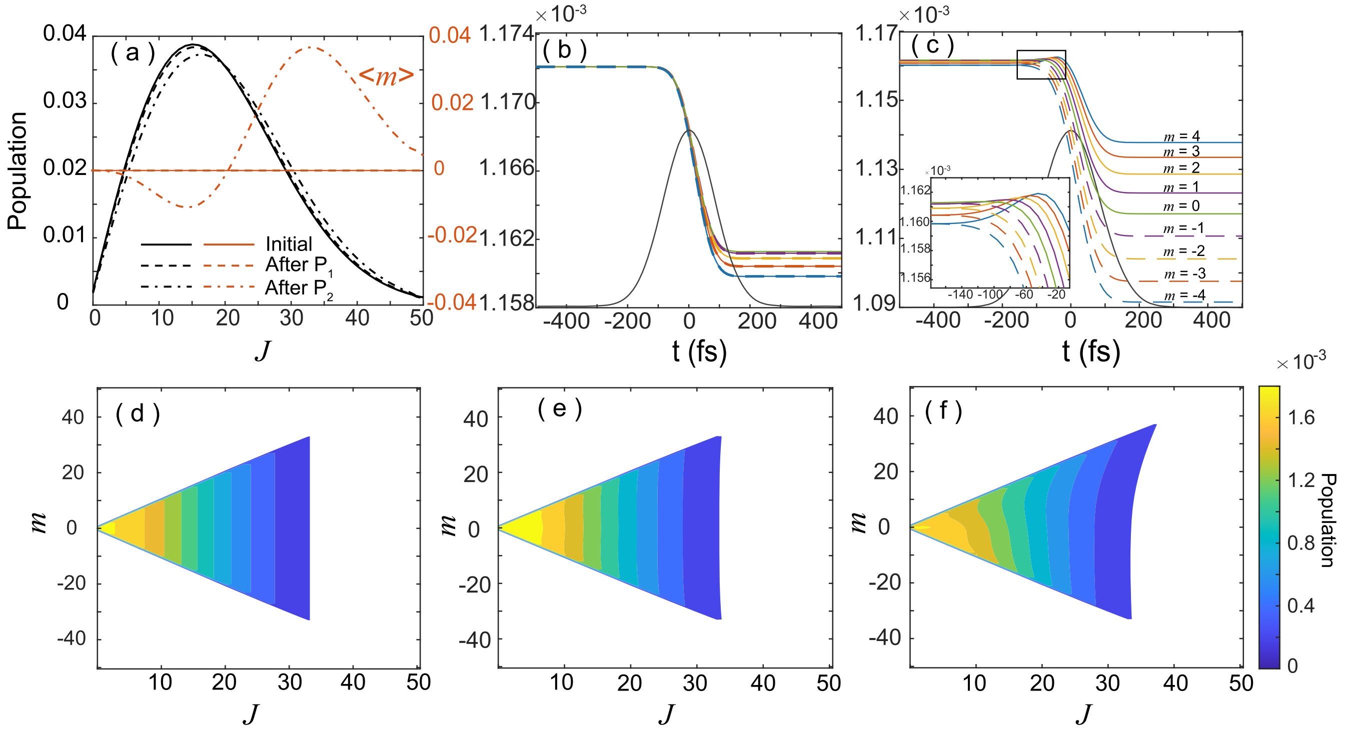

FIG. 5. Numerical results for the change of the population of the overall rotational states. (a) The population distribution of J and the average $\langle m\rangle$ for each J at different times. The population propagation of the initial state $J = 16$ with $m = 0, \pm1, \pm2, \pm3, \pm4$ under (b) the first pump pulse and (c) under the second pump pulse. The population distribution of different rotational states $|J, m\rangle$ (d) at the beginning, (e) after the first pump pulse, and (f) after the second pump pulse.

as shown in the inset of Fig. 5(c). However, as time elapses, all of these states experience a decrease in population. Ultimately, the populations of the opposite m values become well separated. Although the population evolution of different rotational states may have more complexity than depicted in Fig. 5(c), they all exhibit the same trend. The populations of $\pm m$ states diverge during the rising edge of the second pump pulse and become fully separated by the end of the pulse. This asymmetric distribution of $\pm m$ states plays a crucial role in generating the molecular unidirectional rotation.

The contour plots in the second row of Fig. 5 depict the overall population for all m and J at three different times same as Fig. 5(a). At the beginning, shown in Fig. 5(d), the population distribution of different m is initially symmetric around $m = 0$. The population is then transferred to higher J and m levels after the first pump pulse, as can be observed by comparing Fig. 5(d) with Fig. 5(e). The first pump pulse, located along the x axis in our simulation, can induce the $\Delta m = \pm 2$ transition. However, it affects both the $\pm m$ states in the same way, preserving the symmetry of population distribution around $m = 0$. After the second pump pulse, shown in Fig. 5(f), the population distribution of m becomes asymmetric. The population flows from $+m$ to $-m$ for $J < 20$, and from $-m$ to $+m$ for $J > 20$. This asymmetry is also evident in the $\langle m \rangle$ plot in Fig. 5(a).

The above results demonstrate the validity of the present method for obtaining two-dimensional information about rotational motion, providing an approach to observe unidirectional rotation. Furthermore, the underlying excitation processes are elucidated when combined with theoretical simulations. This method is particularly suitable for detecting the motion of complex systems where multiple initial rotational states are involved. For obtaining additional information about the spatial distribution of the RWP, a second weak probe with a different polarization direction can be employed, which can be accomplished by introducing the second probe at a significant incident angle in relation to the first one. For instance, if we use a second probe with a polarization component on the z axis, the distribution information about θ can be obtained. The utilization of a low intensity probe pulse is crucial, as it enables multiple detections of the sample at the same time, with minor changes in its rotational state.

IV. CONCLUSION AND OUTLOOK

We demonstrated an experimental method for visualizing two-dimensional rotational dynamics of molecules at room temperature by employing a rotated WFP detection technique. By adjusting the polarization direction of the pump pulse to match that of the weak probe pulse, we could observe both molecule alignment information and the unidirectional rotation of N_2O at room temperature. The combination of experimental results and theoretical calculations strongly supports the effectiveness of this method, showcasing one of its advantages: its simplicity and ease of implementation. This work makes a contribution to help understanding of molecular dynamics and opens promising applications such as detecting the chiral molecules and superrotors [51]. Furthermore, this method holds the potential for further development, as it can be extended to visualize three-dimensional rotations, which can be achieved by introducing an additional probe pulse with a distinct polarization direction to the pump pulse, specifically applied to asymmetric top molecules at room temperature. Given the ongoing advancements in the field and the increasing interest in understanding and controlling rotational motion [52–54], the current scheme could be useful for visualizing the multi-dimensional rotational dynamics of molecules.

ACKNOWLEDGMENTS

This work was supported by the National Natural Science Foundations of China (NSFC) under Grants No. 12104177, No. 12274470, and No. 61973317, and the Natural Science Foundation of Hunan Province for Distinguished Young Scholars under Grant No. 2022JJ10070.

APPENDIX: ANGULAR VELOCITY OF THE UNIDIRECTIONAL ROTATION

To determine the transient angular velocity of the unidirectional rotation at 19.7 ps, we perform a fitting analysis on the angular distribution at different time delays depicted in Fig. 4(a). The analysis involved obtaining the rotated angle dϕ, around 19.7 ps, along with the corresponding elapsed time dt. Initially, we fit the experimental data using a sinusoidal

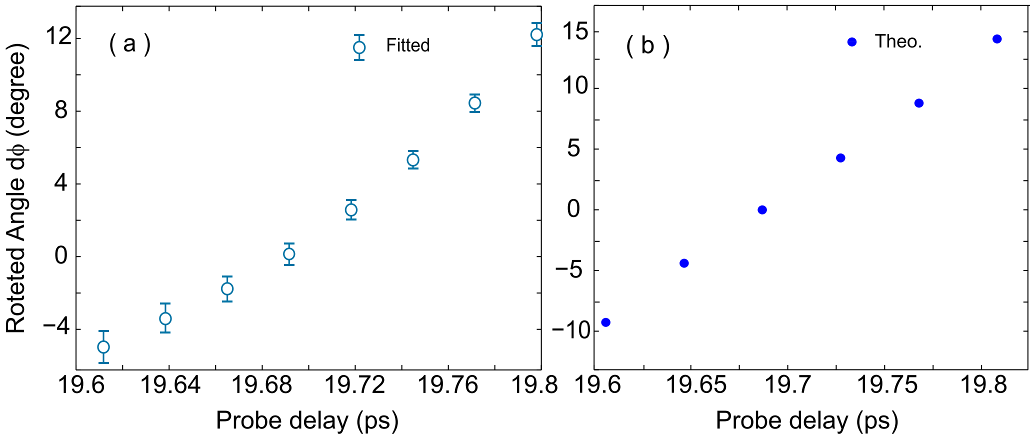

FIG. 6. The rotated angle dϕ of the rotational wave packet at different probe delays around 19.7 ps. (a) Experimental fitted results with 95% confidence interval. (b) Theoretical results.

function to determine the angle ϕ at which the rotational wave packet aligns with different probe delays, resulting in the estimation of the rotated angle dϕ around the delay of 19.7 ps. The fitting results, along with a 95% confidence interval, are presented in Fig. 6. Next, we calculate the transient angular velocity as $\omega = \mathrm{d}\phi/\mathrm{d}t$. For the delay of 19.7 ps, the calculated angular velocity is 1.57×10^{12} rad/s. Furthermore, we apply the same approach to the theoretical data from Fig. 4(e) to determine the theoretical angular velocity, which is 1.98×10^{12} rad/s.

---

[1] H. Stapelfeldt and T. Seideman, Rev. Mod. Phys. **75**, 543 (2003).

[2] C. P. Koch, M. Lemeshko, and D. Sugny, Rev. Mod. Phys. **91**, 035005 (2019).

[3] Q.-Q. Hong, Z.-Z. Lian, C.-C. Shu, and N. E. Henriksen, Phys. Chem. Chem. Phys. **25**, 32763 (2023).

[4] E. Hertz, A. Rouzée, S. Guerin, B. Lavorel, and O. Faucher, Phys. Rev. A **75**, 031403(R) (2007).

[5] A. Rouzée, A. Gijsbertsen, O. Ghafur, O. M. Shir, T. Bäck, S. Stolte, and M. J. J. Vrakking, New J. Phys. **11**, 105040 (2009).

[6] C.-C. Shu and N. E. Henriksen, Phys. Rev. A **87**, 013408 (2013).

[7] E. T. Karamatskos, S. Raabe, T. Mullins, A. Trabattoni, P. Stammer, G. Goldsztejn, R. R. Johansen, K. Długołecki, H. Stapelfeldt, M. J. J. Vrakking, S. Trippel, A. Rouzée, and J. Küpper, Nat. Commun. **10**, 3364 (2019).

[8] C.-C. Shu, Q.-Q. Hong, Y. Guo, and N. E. Henriksen, Phys. Rev. A **102**, 063124 (2020).

[9] Q.-Q. Hong, L.-B. Fan, C.-C. Shu, and N. E. Henriksen, Phys. Rev. A **104**, 013108 (2021).

[10] I. Tutunnikov, L. Xu, Y. Prior, and I. S. Averbukh, Phys. Rev. A **106**, L061101 (2022).

[11] L.-B. Fan, C.-C. Shu, D. Dong, J. He, N. E. Henriksen, and F. Nori, Phys. Rev. Lett. **130**, 043604 (2023).

[12] L.-B. Fan and C.-C. Shu, J. Phys. A: Math. Theor. **56**, 365302 (2023).

[13] S. Fleischer, Y. Khodorkovsky, Y. Prlor, and I. S. Averbukh, New J. Phys. **11**, 105039 (2009).

[14] G. Karras, M. Ndong, E. Hertz, D. Sugny, F. Billard, B. Lavorel, and O. Faucher, Phys. Rev. Lett. **114**, 103001 (2015).

[15] K. Mizuse, K. Kitano, H. Hasegawa, and Y. Ohshima, Sci. Adv. **1**, e1400185 (2015).

[16] A. Korobenko and V. Milner, Phys. Rev. Lett. **116**, 183001 (2016).

[17] A. Owens, A. Yachmenev, and J. Küpper, J. Phys. Chem. Lett. **9**, 4206 (2018).

[18] M. Lapert, E. Hertz, S. Guérin, and D. Sugny, Phys. Rev. A **80**, 051403(R) (2009).

[19] A. A. Milner and V. Milner, Phys. Rev. A **103**, L041103 (2021).

[20] M. Z. Hoque, M. Lapert, E. Hertz, F. Billard, D. Sugny, B. Lavorel, and O. Faucher, Phys. Rev. A **84**, 013409 (2011).

[21] G. Karras, E. Hertz, F. Billard, B. Lavorel, J. M. Hartmann, O. Faucher, E. Gershnabel, Y. Prior, and I. S. Averbukh, Phys. Rev. Lett. **114**, 153601 (2015).

[22] D. Rosenberg, R. Damari, and S. Fleischer, Phys. Rev. Lett. **121**, 234101 (2018).

[23] B. Wang, L. He, Y. He, Y. Zhang, R. Shao, P. Lan, and P. Lu, Opt. Express **27**, 30172 (2019).

[24] Z. Lian, Z. Hu, H. Qi, D. Fei, S. Luo, Z. Chen, and C.-C. Shu, Phys. Rev. A **104**, 053105 (2021).

[25] X. Ren, V. Makhija, and V. Kumarappan, Phys. Rev. Lett. **112**, 173602 (2014).

[26] K. Lin, Q. Song, X. Gong, Q. Ji, H. Pan, J. Ding, H. Zeng, and J. Wu, Phys. Rev. A **92**, 013410 (2015).

[27] K. Lin, P. Lu, J. Ma, X. Gong, Q. Song, Q. Ji, W. Zhang, H. Zeng, J. Wu, G. Karras, G. Siour, J.-M. Hartmann, O. Faucher, E. Gershnabel, Y. Prior, and I. S. Averbukh, Phys. Rev. X **6**, 041056 (2016).

[28] A. A. Milner, J. A. M. Fordyce, I. MacPhail-Bartley, W. Wasserman, V. Milner, I. Tutunnikov, and I. S. Averbukh, Phys. Rev. Lett. **122**, 223201 (2019).

[29] T. Mullins, E. T. Karamatskos, J. Wiese, J. Onvlee, A. Rouzée, A. Yachmenev, S. Trippel, and J. Küpper, Nat. Commun. **13**, 1431 (2022).

[30] J. Qiang, L. Zhou, P. Lu, K. Lin, Y. Ma, S. Pan, C. Lu, W. Jiang, F. Sun, W. Zhang, H. Li, X. Gong, I. S. Averbukh, Y. Prior, C. A. Schouder, H. Stapelfeldt, I. N. Cherepanov, M. Lemeshko, W. Jäger, and J. Wu, Phys. Rev. Lett. **128**, 243201 (2022).

[31] L. Zhou, X. Hu, Y. Peng, J. Qiang, P. Lu, K. Lin, S. Pan, X. Gong, W. Jiang, Z. Jiang, C. Lu, H. Ni, C. Jin, R. Lu, Y. Wu, J. Wang, and J. Wu, Phys. Rev. Lett. **130**, 033201 (2023).

[32] K. Miyazaki, M. Kaku, G. Miyaji, A. Abdurrouf, and F. H. M. Faisal, Phys. Rev. Lett. **95**, 243903 (2005).

[33] L. S. Spector, M. Artamonov, S. Miyabe, T. Martinez, T. Seideman, M. Guehr, and P. H. Bucksbaum, Nat. Commun. **5**, 3190 (2014).

[34] P. Lan, M. Ruhmann, L. He, C. Zhai, F. Wang, X. Zhu, Q. Zhang, Y. Zhou, M. Li, M. Lein, and P. Lu, Phys. Rev. Lett. **119**, 033201 (2017).

[35] L. He, P. Lan, A. T. Le, B. Wang, B. Wang, X. Zhu, P. Lu, and C. D. Lin, Phys. Rev. Lett. **121**, 163201 (2018).

[36] A. Trabattoni, J. Wiese, U. De Giovannini, J. F. Olivieri, T. Mullins, J. Onvlee, S. K. Son, B. Frusteri, A. Rubio, S. Trippel, and J. Küpper, Nat. Commun. **11**, 2546 (2020).

[37] J. Yang, M. Guehr, T. Vecchione, M. S. Robinson, R. Li, N. Hartmann, X. Shen, R. Coffee, J. Corbett, A. Fry *et al.*, Nat. Commun. **7**, 11232 (2016).

[38] Y. Xiong, K. J. Wilkin, and M. Centurion, Phys. Rev. Res. **2**, 043064 (2020).

[39] V. Renard, M. Renard, S. Guerin, Y. T. Pashayan, B. Lavorel, O. Faucher, and H. R. Jauslin, Phys. Rev. Lett. **90**, 153601 (2003).

[40] V. Renard, M. Renard, A. Rouzée, S. Guérin, H. R. Jauslin, B. Lavorel, and O. Faucher, Phys. Rev. A **70**, 033420 (2004).

[41] P. Peng, Y. Bai, N. Li, and P. Liu, AIP Adv. **5**, 127205 (2015).

[42] Z. Lian, S. Luo, H. Qi, Z. Chen, C.-C. Shu, and Z. Hu, Opt. Lett. **48**, 411 (2023).

[43] H. Zhang, B. Lavorel, F. Billard, J. M. Hartmann, E. Hertz, O. Faucher, J. Ma, J. Wu, E. Gershnabel, Y. Prior, and I. S. Averbukh, Phys. Rev. Lett. **122**, 193401 (2019).

[44] J. Ma, H. Zhang, B. Lavorel, F. Billard, E. Hertz, J. Wu, C. Boulet, J. M. Hartmann, and O. Faucher, Nat. Commun. **10**, 5780 (2019).

[45] M. Bournazel, J. Ma, F. Billard, E. Hertz, J. Wu, C. Boulet, J.-M. Hartmann, and O. Faucher, Phys. Rev. A **107**, 023115 (2023).

[46] J. Bert, E. Prost, I. Tutunnikov, P. Béjot, E. Hertz, F. Billard, B. Lavorel, U. Steinitz, I. S. Averbukh, and O. Faucher, Laser Photonics Rev. **14**, 1900344 (2020).

[47] I. Tutunnikov, E. Prost, U. Steinitz, P. Béjot, E. Hertz, F. Billard, O. Faucher, and I. S. Averbukh, Phys. Rev. A **104**, 053113 (2021).

[48] S. Ramakrishna and T. Seideman, Phys. Rev. A **87**, 023411 (2013).

[49] G. Zeng, C. Wu, H. Jiang, Y. Gao, N. Xu, and Q. Gong, J. Phys. B: At. Mol. Opt. Phys. **42**, 165508 (2009).

[50] Y. Gao, C. Wu, N. Xu, G. Zeng, H. Jiang, H. Yang, and Q. Gong, Phys. Rev. A **77**, 043404 (2008).

[51] I. Tutunnikov, E. Gershnabel, S. Gold, and I. S. Averbukh, J. Phys. Chem. Lett. **9**, 1105 (2018).

[52] R. Tehini, K. Hamraoui, and D. Sugny, Phys. Rev. A **99**, 033419 (2019).

[53] E. J. Zak, A. Yachmenev, and J. Küpper, Phys. Rev. Res. **3**, 023188 (2021).

[54] H. Chadwick, M. F. Somers, A. C. Stewart, Y. Alkoby, T. J. D. Carter, D. Butkovicova, and G. Alexandrowicz, Nat. Commun. **13**, 2287 (2022).